



PAPER



Cite this: *Soft Matter*, 2017, 13, 7412

Tunable hydrodynamics: a field-frequency phase diagram of a non-equilibrium order-to-disorder transition†

Somayeh Khajepour Tadavani * and Anand Yethiraj *

We present experiments on a model system consisting of dielectric (silicone oil) drops in a “leaky dielectric” (castor oil) carrier fluid that exhibits dynamic non-equilibrium phases as a function of the amplitude and frequency of an external AC electric field. At high frequencies, the dielectric drops are pinned to a periodic lattice by dielectrophoretic forces induced by a patterned bottom electrode. Beginning with this state of imposed order, we examine the processes that take this system from order to disorder, with decreasing frequency corresponding to an increase in the range of the hydrodynamic forces. We find two kinds of disorder, shape- and translational disorder, that occur in frequency–amplitude space. We also find regimes where drop breakup is dominant, and where order/disorder of large drops can be probed without significant drop breakup. With decreasing frequency (*i.e.*, increasing hydrodynamic coupling between drops) and on timescales from seconds to minutes, the drops exhibit motion that resembles Brownian motion of particles in a crystal, with an effective temperature that increases with the strength of the electrohydrodynamic driving force. In this limit, the system behaves like a thermal system and the lattice is seen to melt at an effective Lindemann parameter of $L_{\text{eff}} \sim 0.08$. This non-equilibrium thermodynamics, probed on timescales from seconds to minutes, likely arises from the pseudo-random velocity fields in the carrier fluid, as evidenced by the fractional, $t^{3/2}$, super-diffusive tracer dynamics at shorter timescales.

Received 8th June 2017,
Accepted 19th September 2017

DOI: 10.1039/c7sm01145h

rsc.li/soft-matter-journal

1 Introduction

Self-organization in colloidal systems has uncovered new phases that arise from competition between entropy and tunable interactions between building blocks;^{1–5} controlling interactions has been a powerful means to examine the nature of crystal phases and phase transitions.^{6–10} While there remain significant challenges to making highly ordered structures,^{11,12} controllable disorder also has applications in natural systems: examples are the role of amorphous structures in biomineralization¹³ and the role of disorder in the brilliant whiteness in beetle scales.¹⁴ Thus, a better understanding of self-organization either in systems with greater complexity or in systems farther from equilibrium is necessary.

Self-organization in systems with greater complexity has been explored in Brownian colloidal suspensions by examining anisometric particle shape,^{15–17} and soft and floppy microgel particles^{18,19} as well as particles with anisotropic^{6,20} and patchy interactions.^{21,22}

In all these cases, the goal has been monodispersity in particle geometry, in order to keep the systems simple.

An understanding of non-equilibrium phase transitions is also relevant in biological systems: here, two examples are the relevance of principles of polymer physics inside cells,^{23,24} and the relevance of model active matter systems^{25,26} for transport processes within cells. Granular systems with building blocks of size 10 μm or greater are invaluable as model systems that extend the statistical physics of phase transitions to non-Brownian systems;^{27–29} this includes studies with single-particle resolution of dynamical phase transitions such as jamming. However, a key ingredient in biological cells is the existence of soft liquid–liquid interfaces and the formation of compartments with or without membranes.³⁰ In contrast with colloidal suspensions, even the particle size in liquid–liquid emulsions is achieved by self-organization, so they are inherently more complex.

A recently introduced model system in a liquid–liquid emulsion³¹ with drop size on the 10–100 μm scale is directly tunable *via* an electrically driven hydrodynamic interaction. Decreasing the frequency of the driving electric field has been shown to enhance the hydrodynamic coupling between the drops,³¹ with multiscale flows reminiscent of turbulence

Physics and Physical Oceanography, Memorial University of Newfoundland, St. John's, NL, A1B 3X7, Canada. E-mail: skt660@mun.ca, ayethiraj@mun.ca

† Electronic supplementary information (ESI) available. See DOI: 10.1039/c7sm01145h

observed in the zero-frequency (d.c.) limit.^{32,33} Moreover, non-uniform fields have been employed to create periodic droplet arrays for microlens applications.³⁴ This tunability of collective behaviors suggests that it could be valuable as a non-equilibrium model system: this is the focus of the current study. Aqueous media have been employed as well in order to induce and control structure formation using electrohydrodynamics,^{35–38} so the concepts developed in this system could be transferred to aqueous environments.

In this study we employ a time-varying external AC electric field with two control parameters, the amplitude and the frequency, to examine non-equilibrium order-to-disorder processes in a hexagonal array of silicone oil drops, as an internal liquid, surrounded by castor oil, as a partially charged external liquid. For a two-dimensional array of drops, we study the shape deformation of drops, as well as their translational and orientational dynamics, as the driving force is increased in two ways, either by increasing field amplitude or by decreasing frequency.

2 Methods and techniques

2.1 Samples and hardware

Fig. 1(a) shows the side view of a test cell with the electric field perpendicular to the microscope slide (*i.e.* perpendicular to our field of view) and parallel to gravity. Two indium tin oxide, ITO, coated cover glass slides are separated by glass spacers with defined thickness of $h = 140 \mu\text{m}$. As shown in Fig. 1(b), the ITO bottom plate is selectively etched by photo-lithography such that a hexagonal array of roughly circular ITO-free regions, diameter $\sim 50 \mu\text{m}$ and with nearest-neighbor center-to-center spacing $d_{\text{nn}} \sim 100 \mu\text{m}$, is obtained. The plates and spacers are held together with ultraviolet-curable epoxy, Norland Optical Adhesive 61 and 68. The ITO slides are optically transparent and electrically conductive, which enables their use as electrodes and imaging through them as with regular glass. The cell is filled by pipetting an emulsion of silicone oil, dielectric constant $\epsilon_{\text{in}}/\epsilon_0 = 2.4$, conductivity $\sigma_{\text{in}} = 3.95 \times 10^{-11} \text{ S m}^{-1}$, and viscosity $\mu_{\text{in}} = 0.137 \text{ Pa s}$, and castor oil, dielectric constant $\epsilon_{\text{ex}}/\epsilon_0 = 3.6$, conductivity $\sigma_{\text{ex}} = 4.0 \times 10^{-10} \text{ S m}^{-1}$, and viscosity $\mu_{\text{ex}} = 0.819 \text{ Pa s}$, in a volume ratio of 1 : 16. The subscripts “in” and “ex” are used to represent the droplet and the suspending fluid, respectively. The lateral dimension of the cells is $\sim 0.75 \text{ cm}$.

A sinusoidal AC voltage, Tektronix model AFG3022, is applied to the cell, while the output voltage of the power generator is amplified by a high voltage amplifier, Trek model PZD2000A. Bright field microscopy is used to observe and record the image sequences.

2.2 Image processing

The long-time dynamics of trapped droplets, located on the etched-out patterns, is studied by filtering out the periodic oscillations *via* the expedient of stroboscopic imaging at the frequency of oscillation. The usefulness of this technique has been shown in Fig. 1(c) by 6 snapshots at equal intervals within a full cycle of oscillation at 3 Hz. The first and last frames are

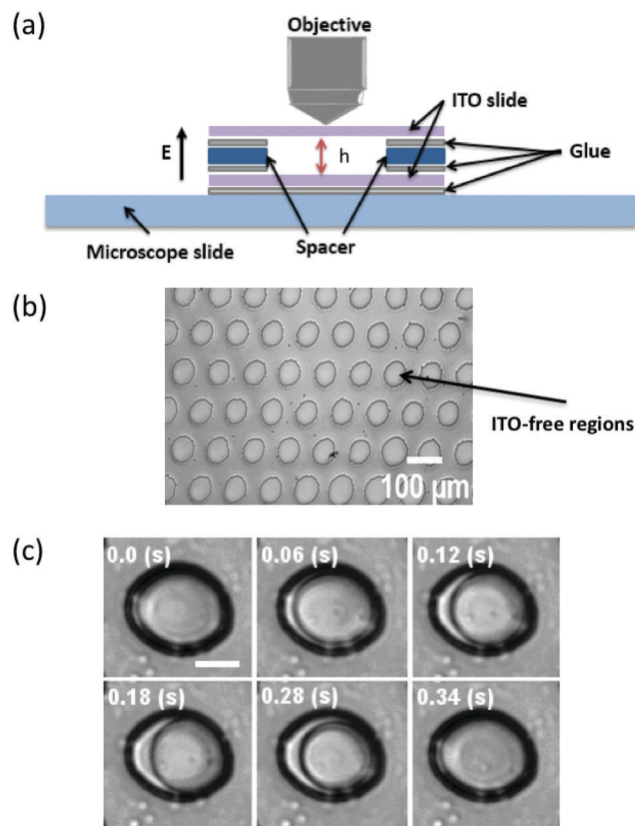


Fig. 1 (a) A schematic design: side view of the cell geometry. (b) Bottom electrode with ITO-free regions shown by circles. (c) Drop shape within one field cycle. When one images a drop rapidly, one sees periodic oscillations at intermediate times of 0.06, 0.12, 0.18 and 0.28 s between the two maximums of oscillation, at 0 s and 0.34 s. The dark edges show the edge of the circular pattern and overlaid droplets. At intermediate times, the edges of the drops are not overlaid on the edge of the patterns. $f = 3 \text{ Hz}$, $E = 5.6 \text{ V } \mu\text{m}^{-1}$ and is perpendicular to the page. Scale bar is $25 \mu\text{m}$.

the beginning and end of the cycle, while the four intermediate oscillations are ignored in the strobe technique.

The second channel of the AC function generator produces a square wave with the driving frequency and a peak-to-peak amplitude of 2.5 V in order to trigger image acquisition by the camera. To get the maximum of drop deformation a phase difference of $+90^\circ$ between the two periodic waves is applied to the sinusoidal wave while the bottom and top electrodes are connected to the negative and positive electrodes, respectively.

After recording the experiment, the shape deformation and positions of the droplets are studied. A typical field of view (such as those shown in Fig. 4) consists of 21 drops. All the analyses were repeated in different regions of the same cell and also for a new cell with the thickness roughly equal to the current cell. To lowest order, a deformed circle may be approximated as an ellipse. An ellipse-fitting algorithm (<http://www.asu.cas.cz/sos/software/mpfitellipse.pro>), written in IDL (Interactive Data Language) is used to fit an approximate ellipse to the points forming the drops in a binary image. The output consists of the major axis M , the minor axis m , centroid (x, y) , and the angle of the major axis with respect to the x -axis.

The shape deformation of the drop is quantified by the unitless “roundness”,

$$R = 4A_{cs}/(\pi M^2) = 1/S, \quad (1)$$

where the area $A_{cs} = \pi Mm/4$ and $S = M/m$ is the aspect ratio of the drop. R can vary between 0 and 1 with unity representing perfectly round objects. Using the centroid of the fitted ellipse, one is also able to track droplet motion using standard particle tracking techniques.³⁹ From this, we obtain (Section 4.4) the 2D mean square displacement, $\langle \Delta r^2 \rangle$, where r is the magnitude of the displacement of each ellipse as a function of the time t (from a reference start time t_0), and $\langle \cdot \rangle$ is an average over all the ellipses in the system, and over the reference time. Using the centroid of the drops, one can also obtain the pair correlation function, $g(r)$, and bond order parameter, $\langle \Psi_6 \rangle$.

The time correlation of drop orientations, obtained for different frequencies and amplitudes using an auto-correlation function, is implemented in IDL (http://www.harrisgeospatial.com/docs/A_CORRELATE.html).

2.3 Brief summary of experiments

The silicone oil drops are prepared prior to each experiment so that they are located, using the negative dielectrophoretic force, described in Section 3.2, at the patterned holes in the ITO-film electrode and have a diameter of 50 μm . While the cell has a thickness of 140 μm , there is free space (filled with the leaky dielectric, castor oil) above the silicone oil drop, which thus assumes the shape of a section of a hemisphere, which from the top view is circular.

$$\Phi = \frac{9}{16} \times \left(1 - \frac{H^{-1}(11N + 14) + H^{-2}(15(N + 1) + S(19N + 16)) + 15\tau^2\omega^2(1 + N)(1 + 2S)}{10(1 + N)((2H^{-1} + 1)^2 + \tau^2\omega^2(S + 2)^2)} \right). \quad (3)$$

The non-deformed state of each drop is roughly hemispherical; this is the drop shape at low amplitudes or high frequencies. In our experiments, we hold the electric field amplitude fixed and observe the time dependence of drop deformations for a sweep of frequencies. Then, we change the amplitude and repeat the experiment. For each experiment, we image the drop stroboscopically (except in Section 4.5 where we probe dynamics at times much shorter than one period of the sinusoidal electric field oscillation). The drop is imaged close to the bottom substrate, 10 μm above it, in order to put the edge of the ITO pattern area out of focus and yet not change the detected drop area significantly.

3 Background and theory

In order to incorporate tunable hydrodynamics into a model granular crystal we combine three elements: electrohydrodynamics in a two-fluid emulsion, dielectrophoresis as a means of droplet trapping, and a methodology to measure displacement fluctuations in a crystal. In what follows, we present the related background concepts.

3.1 Electrohydrodynamics of two-fluid emulsions

In an emulsion of two immiscible dielectric liquids (“internal” and “external”), the shape of a drop of the internal liquid is

spherical in the absence of external forces due to the minimization of surface energy. An external electric field induces bound polarization charge resulting in a force normal to the liquid–liquid interface that changes the shape to a prolate ellipsoid. This shape deformation occurs when the dimensionless electric capillary number, which is a ratio of electric forces and restoring interfacial tension acting on a drop, *i.e.*, $\text{Ca}_E \sim \epsilon_{\text{ex}} a E^2 / \gamma$, is comparable to unity. In a suspension composed of a dielectric internal fluid and a “leaky dielectric” external fluid with large enough ionic conductivity, σ_{ex} , an electric field results in continuous steady-state electrohydrodynamic flows. In an AC electric field, the field amplitude and frequency can both be utilized to tune the strength and the range of the resulting electrohydrodynamic (EHD) interactions. The generic behavior is rather well described by the lumped-parameter leaky dielectric model (LDM)^{40–42} which ignores the finite Debye screening length at the liquid–liquid interfaces.⁴³ The deformations of the internal liquid are characterized by a balance of three forces: the bound polarization charge (normal to the interface), the induced free charge (normal and tangential to the interface), and viscous forces (also normal and tangential to the interface).⁴³ The drop deformation $D = (d_{\parallel} - d_{\perp}) / (d_{\parallel} + d_{\perp})$ can be measured experimentally, and may be related to the system parameters:

$$D = \Phi \frac{a \epsilon_{\text{ex}} E^2}{\gamma}, \quad (2)$$

where a is the radius of a non-deformed drop and Φ is a shape-discriminating function that is given by

Φ may be used to classify deformations as non-spherical (prolate or oblate), or spherical.⁴² In eqn (3), for our system, $S = \frac{\epsilon_{\text{in}}}{\epsilon_{\text{ex}}} = 0.67$,

$$H = \frac{\sigma_{\text{in}}}{\sigma_{\text{ex}}} = 0.10, \quad N = \frac{\eta_{\text{in}}}{\eta_{\text{ex}}} = 0.17, \quad \tau = \frac{\epsilon_{\text{ex}}}{\sigma_{\text{in}}} = \frac{\epsilon_0 k_{\text{ex}}}{\sigma_{\text{in}}} \simeq 0.81 \text{ s}, \quad \omega = 2\pi f.$$

The parameters ϵ , σ , and η are absolute permittivity, conductivity, and viscosity of liquids respectively, while k and ϵ_0 are the relative permittivity and the vacuum permittivity respectively. The frequency of the field f is the only variable in the equation. The subscripts “in” and “ex” are used to represent the droplet and the surrounding fluid, respectively. Prolate and oblate deformations result when $\Phi > 0$ and $\Phi < 0$ respectively, while the drop stays spherical when $\Phi = 0$. Fig. 2(a) represents Φ versus f for the current system, where the crossover frequency from oblate to prolate is roughly 6.1 Hz.

The strength of EHD forces, and the strength of the resulting drop deformations, is governed by the electric field amplitude. Feng⁴⁴ wrote a modified electric capillary number for EHD using the maximum velocity assuming creeping flows around a non-deformed drop,

$$\text{Ca}_E^0 \equiv \frac{9|S^{-1}H - 1|N^{-1} \epsilon_{\text{in}} a E^2}{10(H + 2)^2(N^{-1} + 1) \gamma}, \quad (4)$$

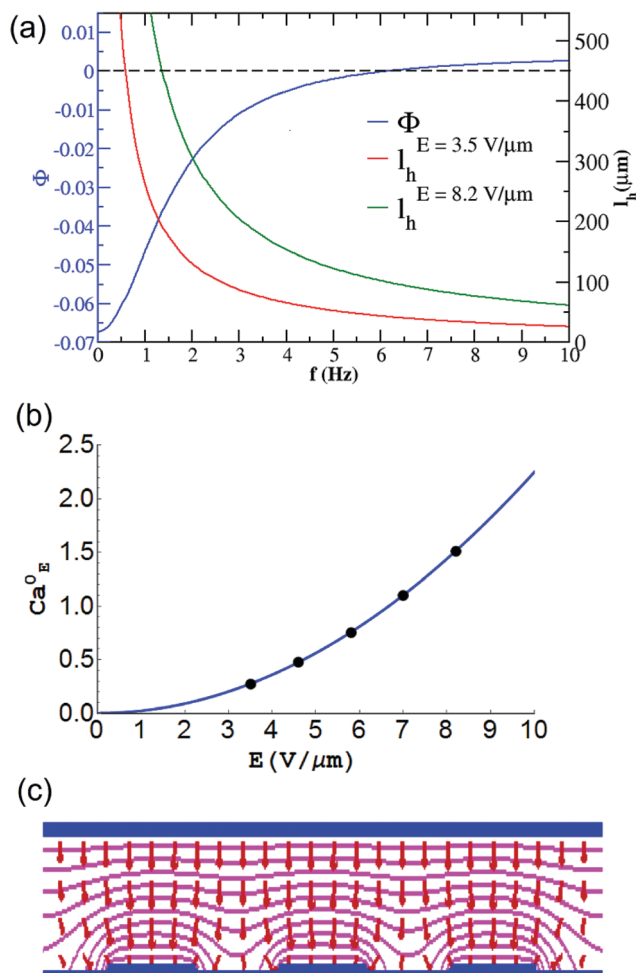


Fig. 2 (a) The shape-discriminating function, Φ , is greater than zero at high frequency (prolate drops), but becomes negative (oblate drops) at roughly 6 Hz. The hydrodynamic length, l_h decreases inversely with frequency, but increases proportionally with field amplitude. (b) Electric capillary number, Ca_E^0 , versus electric field amplitude, E . As Ca_E^0 approaches unity, the smooth liquid–liquid interface should destabilize and lead to drop breakup. The points indicate the experimental field values used. (c) Simulation of electric field in a cell with a uniform top conducting electrode and a bottom electrode with non-conducting holes. The low electric field regions have less dense equipotential lines and smaller electric fields vectors (denoted by arrows). The gradient of this non-uniform electric field forces the liquid with lower dielectric constant, ϵ , into low electric field regions.

where $\gamma \simeq 3\text{--}4 \text{ mN m}^{-1}$ is the interfacial tension between the oils, $\epsilon_{\text{in}} = \epsilon_0 k_{\text{in}} = 21.24 \times 10^{-12} \text{ F m}^{-1}$, a is the radius of the non-deformed drop and E is the strength of the field. For the current system, we can write $\text{Ca}_E^0 = 0.9 \times 10^{-9} a E^2$ where $a = 25 \mu\text{m}$ is the initial drop radius (a and E are expressed in mks units). The superscript “0” refers to the electric Capillary number at the initial drop diameter. Variation of Ca_E^0 versus E is plotted in Fig. 2(b); also shown are circles representing the values of electric field amplitude used in this work.

The range of the electrohydrodynamic (EHD) interactions can be modulated by changing the frequency, f . Varying f affects the lengthscale of hydrodynamics interactions, $l_h = v_d/f$, where

$v_d = \mu_E E$ is the ionic drift velocity, which is set by the electric mobility μ_E and the electric field, E . The electric mobility in turn is $\mu_E = z_i e_0 / 6\pi r \eta_{\text{ex}}$,⁴⁵ where $z_i e_0$ is the ions’ charge, and r is the radius of the ions. The electric mobility of the current system $\mu_E \simeq 75 \mu\text{m}^2 \text{ V}^{-1} \text{ s}^{-1}$. Fig. 2(a) shows the inverse relation of the hydrodynamic length versus frequency for two field amplitudes. At the crossover frequency of $\approx 6 \text{ Hz}$, l_h is $< 50 \mu\text{m}$ for $E = 3.5 \text{ V } \mu\text{m}^{-1}$ and $\approx 100 \mu\text{m}$ for $E = 8.2 \text{ V } \mu\text{m}^{-1}$; *i.e.*, it is smaller than and equal to, respectively, the drop nearest-neighbor spacing $d_{\text{nn}} = 100 \mu\text{m}$, while at 2 Hz, $l_h > d_{\text{nn}}$ for all field amplitudes probed. The frequency regime below 6 Hz is therefore where we expect interesting electrohydrodynamic behaviors.

Φ is a function of frequency (and not field amplitude), while the electric Capillary number, Ca_E^0 , is a function of field amplitude (and not frequency). Both control deformation of individual drops. The hydrodynamic length, l_h , which is a function of both, defines the lengthscale over which drops couple with neighboring drops.

3.2 Dielectrophoretic trapping of drops

We employ dielectrophoresis to prepare a periodic lattice of drops, using methods demonstrated previously.³⁴ A patterned electrode creates a non-uniform electric field. A dielectric drop in a dielectric liquid responds to the field non-uniformly *via* the dielectrophoretic force, F_{DEP} ,

$$F_{\text{DEP}} = \frac{1}{2}(\epsilon_{\text{in}} - \epsilon_{\text{ex}})\nabla(\mathbf{E} \cdot \mathbf{E}), \quad (5)$$

which, in the long-time steady state, creates a spatially localized array of silicone oil drops in castor oil, or more generally, a patterned arrangement of two immiscible dielectric liquids with different dielectric constants.³⁴ Fig. 2(c) shows a simulation (using Poisson Superfish http://laacg.lanl.gov/laacg/services/serv_codes.phtml) of the equipotential lines, as well as the electric field amplitude and direction (vectors on a grid) above a patterned electrode. The region with holes in the conducting surface has sparse collections of equipotential lines as well as vectors with the most rapidly changing amplitude, and this region attracts the oil with a lower dielectric constant. These holes in the bottom electrode are thus a trap for the silicone oil, and thus make this system quasi-two-dimensional.

3.3 Bond-orientational order

Order and disorder in two dimensions are characterized by a bond-orientational order parameter.⁴⁶ For 6-fold symmetric structures, such as the symmetry of the periodic lattice imposed by dielectrophoretic methods in this work, the relevant order parameter is

$$\Psi_6 = \left| \frac{1}{N} \frac{\sum_{j=1}^N l_j e^{i6\theta_j}}{\sum_{j=1}^N l_j} \right|, \quad (6)$$

where N is the number of nearest neighbors at drop j , l_j is the line segment that connects the neighbors $j - 1$ and j , and θ_j is the angle that the vector from the selected drop to the j th

neighbor makes with respect to the x axis.^{47,48} Ψ_6 can vary between 0 and 1, with 1 indicating perfect 6-fold symmetry. For drops designated as 6-fold sites ($\Psi_6 > 0.7$), $\langle \Psi_6 \rangle$ is calculated in one frame and then averaged over an image stack that represents a time series.

3.4 Study of dynamics in a soft crystal

When electric fields are applied in our leaky dielectric model system, they generate pseudo-random flows in the carrier fluid. These flows, in turn, generate drop motions, which can be examined as if it were effective self-diffusion.³³ Since we have drops on a lattice in this work, we examine our system by employing an analog to that of colloid diffusion in a crystal lattice.

In a fluid and in a crystal, the mean-squared displacements of atoms yield important information: the self-diffusivity in a fluid, and the elastic constant in a crystal. In soft crystals, and in two dimensions, one can write the mean-squared displacement (MSD), following Weiss *et. al.*,⁴⁹ as

$$\text{MSD} = \langle (r(t) - r(0))^2 \rangle = \frac{\beta k + \frac{1}{4Dt}}{\left(\frac{\beta k}{2} + \frac{1}{4Dt}\right)^2}, \quad (7)$$

where $\beta^{-1} = k_B T$, k is the spring constant, D is the effective diffusion coefficient, and t is time. At $t \rightarrow 0$, the behavior is simply diffusive: $\text{MSD}_{t \rightarrow 0} = 4Dt$. Owing to the stroboscopic imaging, the shortest time probed is $t = 1/f$, and we have limited data with which to access short time behavior to extract the effective diffusivity D ; however, the asymptotic long-time value of the MSD yields

$$\text{MSD}_{t \rightarrow \infty} = \langle (r(t) - r(0))^2 (t \rightarrow \infty) \rangle = \frac{4}{\beta k}. \quad (8)$$

A similar interplay of linear time dependence followed by a plateau is observed in colloids (which display Brownian diffusion) in the presence of an optical trap (which acts as a harmonic restoring force⁵⁰ at least at small trapping strengths⁵¹). One may relate the long-time saturation value of the MSD with an effective Lindemann parameter

$$L_{\text{eff}} = \frac{1}{d_{\text{nn}}} \sqrt{\frac{3}{4} \text{MSD}_{t \rightarrow \infty}} = \frac{1}{d_{\text{nn}}} \sqrt{\frac{3}{\beta k}}, \quad (9)$$

where d_{nn} is the crystal nearest-neighbor distance.⁵²

4 Results and discussion

4.1 Electrohydrodynamic drop deformation

In the presence of an external AC electric field, for frequencies below the crossover frequency shown in Fig. 2(a) where $\Phi < 0$, a silicone oil drop becomes oblate, *i.e.*, it undergoes vertical compression, and thus expands laterally. The two-dimension, lateral view of this time-dependent, periodic expansion can either be symmetric and circular or non-circular, depending on the strength of the driving field, but it is roughly periodic due to the time-dependence of the AC electrohydrodynamic forces. By imaging the system stroboscopically, one can follow subtle

deviations from periodicity in the long-time lateral orientational and translational dynamics of the drops, once per cycle, as a function of the amplitude and frequency of the driving electrohydrodynamic forces.

One can measure Φ experimentally using eqn (2). When a uniform sphere becomes an oblate spheroid, the lateral cross-sectional image shows a circle with increased area. To measure D from 2D snapshots, one needs to measure d_{\parallel} (*i.e.*, parallel to the vertical electric field) and d_{\perp} (in the image plane, which is perpendicular to the vertical electric field). In actual fact, in the image plane the drop is a deformed circle which can be approximated as an ellipse. A fit therefore yields two values, $d_{1\perp} = M/2$ and $d_{2\perp} = m/2$, where M and m are the major and minor axes of an ellipse with area $A_{\text{cs}} = \pi d_{1\perp} d_{2\perp} = \pi Mm/4$.

The snapshots of a drop shown in Fig. 3(b) ($E = 5.8 \text{ V } \mu\text{m}^{-1}$) show that with decreasing frequency, the drops become larger in cross section and also increasingly non-circular. Below 1 Hz in Fig. 3(c), the drop shrinks in size due to the breakoff of tiny droplets from the large drops. The sudden increase or decrease in area of the drops at low frequencies is due to the breakup/coalescence of droplets. The variation of the fitted ellipse cross-sectional area, A_{cs} , of a drop at different frequencies is plotted in Fig. 3(c) for the field amplitudes employed in this work. While A_{cs} is roughly the same at high frequencies for all field amplitudes, with decreasing frequency there is first an increase, corresponding to a shape change from spherical to oblate spheroidal. This larger cross-section correlates with a smaller vertical extent due to volume conservation of the drop.

For a non-deformed drop, close to the crossover frequency, where $a = d_{\parallel} = d_{1\perp} = d_{2\perp}$, the volume can be measured using $V_0 = 4\pi a^3/3$. By lowering the frequency, before the breakup of the drop, a spherical drop changes into an ellipsoid, while the volume of the drop stays constant, $V_{\text{ellipsoid}} = V_0$, so one can measure $d_{\parallel} = V_0/(4\pi d_{1\perp} d_{2\perp}/3) \equiv V_0/(4A_{\text{cs}}/3)$. In addition, we may simply obtain d_{\perp} using $d_{\perp} = \sqrt{A_{\text{cs}}/\pi}$. The experimental values of Φ , obtained from the experimental D using eqn (3), are shown in Fig. 3(d) (the symbols refer to experiments at different electric field amplitudes), and are in good agreement with the theoretical value (solid black curve) in both the crossover frequency, ≈ 6 Hz, and the decrease in the amplitude of Φ at low frequency.

4.2 An order-disorder transition

Fig. 4 shows pictorially the field- and frequency-dependence of an order-to-disorder transition in a silicone oil drop array in a castor oil background. A snapshot from each value of amplitude and frequency may be observed in ESI,† Movie S1. At each field amplitude, we see the effect of lowering the AC frequency, and thus increasing the hydrodynamic length. For the lowest field amplitude reported ($E = 3.5 \text{ V } \mu\text{m}^{-1}$, $\text{Ca}_E^0 \approx 0.27$), we find that upon decreasing the frequency from 8 Hz to 0.2 Hz (top to bottom in the first vertical panel in Fig. 4) we see a modest increase in cross-sectional area of the drop (purple circles in Fig. 3(c)). The drops are also slightly more displaced from their equilibrium position at the lowest frequencies, driven by fluid

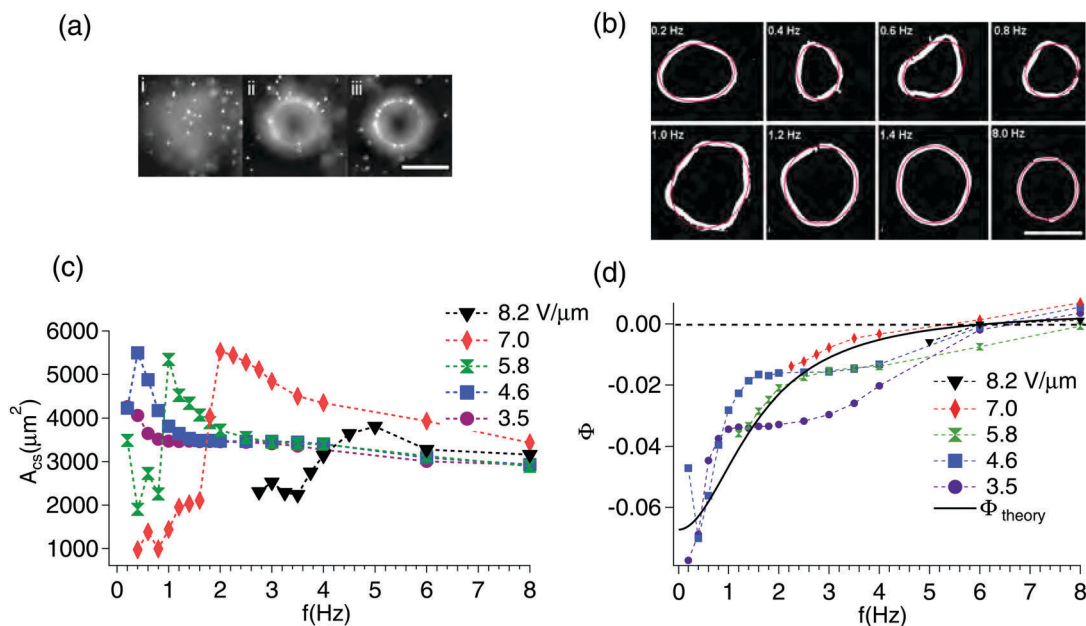


Fig. 3 (a) A silicone oil drop in an emulsion of castor oil with fluorescent PMMA tracer particles is imaged at (i) 110 μm , (ii) 10 μm and (iii) 0 μm from the bottom electrode by fluorescence microscopy. The drop is roughly hemispherical and does not touch the top electrode. $f = 8 \text{ Hz}$, $E = 7.0 \text{ V } \mu\text{m}^{-1}$, perpendicular to the page. Scale bar is 50 μm . (b) A binarized image of the drop at the first few lower (0.2, 0.4, 0.6, 0.8, 1.0, 1.2, 1.4 Hz) and the highest (8.0 Hz) frequencies with the fitted ellipse overlaid in red. $E = 5.8 \text{ V } \mu\text{m}^{-1}$ and is perpendicular to the page. Scale bar is 50 μm . (c) Variation of the fitted ellipse lateral cross-sectional area, A_{cs} , of one drop with frequency, for different field amplitudes. (d) Experimental plot of Φ , obtained from 2D images of deformed droplets at different electric fields. A good agreement between the observations and the theoretical expectation for the frequency dependence is observed, both in terms of (the negative to positive) crossover frequency and magnitude of Φ .

motion; this can be deduced qualitatively from the motion of a black dust particle (observed at different locations in the 1, 0.8, and 0.2 Hz graphics).

At a higher field amplitude ($E = 4.6 \text{ V } \mu\text{m}^{-1}$, $\text{Ca}_E^0 \approx 0.48$), one observes by decreasing the frequency from 8 Hz to 0.8 Hz (top to bottom in the second left vertical panel in Fig. 4) that drops not only have larger lateral area (blue squares in Fig. 3(c)), but that below a threshold frequency, the circular droplets changed into faceted drops, going from circular to polygonal, at 0.6 and 0.4 Hz and then to disordered and random shapes at 0.2 Hz. No drop breakup/coalescence is observed for $E = 3.5 \text{ V } \mu\text{m}^{-1}$ and $E = 4.6 \text{ V } \mu\text{m}^{-1}$.

At the next higher field ($E = 5.8 \text{ V } \mu\text{m}^{-1}$, $\text{Ca}_E^0 \approx 0.76$) one new element is introduced: the breakup. This is observed at and below 1 Hz (middle panel in Fig. 4): the darker spots in Fig. 4 are locations of drop breakup, and drops get depinned from their trap locations. There is a balance between breakup of larger drops and coalescence of smaller droplets, with the end result being a shift of the peak in the drop size distribution to smaller values; this has been discussed in earlier work.^{32,33} With the consequent reduction in drop size and Ca_E^0 , the polygonal shapes are transformed to curved-edge shapes at 0.8 Hz. For 0.4 Hz and 0.2 Hz, the drops appear rather detached from the traps.

At $E = 7.0 \text{ V } \mu\text{m}^{-1}$ ($\text{Ca}_E^0 \approx 1.1$) (the fourth vertical panels in Fig. 4), much the same behavior is observed, except at a higher frequency of about 2.0 Hz. Similarly, the polygonal deformation is observed from 2.75 to 2.0 Hz, followed by curved-edge shapes from 1.8 Hz to 1.4 Hz.

At the highest field, however, $E = 8.2 \text{ V } \mu\text{m}^{-1}$ ($\text{Ca}_E^0 \approx 1.51$), rather than a transition from circular to polygonal, one observes orientational deformation between 5.0 and 3.5 Hz. The increase in drop area (black triangles in Fig. 3(c)) is also much less pronounced than for lower field amplitudes, owing to earlier onset of drop breakup. Drop breakup and coalescence are nevertheless observed at frequencies below 4 Hz.

One can quantify these observations by tracking the height of the first peak of the pair correlation function, $g(\sigma)$, and the roundness, R (defined in eqn (1)), of droplets as a function of frequency and amplitude: these are shown in Fig. 5(a) and (b), respectively. A common transition at all field amplitudes is a transition to non-circular lateral drop shapes with decreasing frequency, which is followed by depinning of drops from their trapped positions at slightly lower frequency: the latter correlates with a decrease in the height of the nearest neighbor peak. This happens (filled circles in Fig. 5(b)) at 4.5 Hz at $E = 8.2 \text{ V } \mu\text{m}^{-1}$ and 0.6 Hz at $E = 4.6 \text{ V } \mu\text{m}^{-1}$. For all fields above $E = 3.5 \text{ V } \mu\text{m}^{-1}$, the roundness reaches a low value between 0.75 and 0.85. The highest field ($E = 8.2 \text{ V } \mu\text{m}^{-1}$) is different, because there is a fall with decreasing frequency in roundness, first near 3.75 Hz, then an increase, then a second decrease near 2 Hz.

In general, the non-monotonic increase in R likely arises from a decrease in Ca_E due to a reduction in drop size after breakup. The dynamics of the droplets close to the frequency threshold separating circular from non-circular droplets is observed for different field amplitudes in ESI,[†] Movie S2.

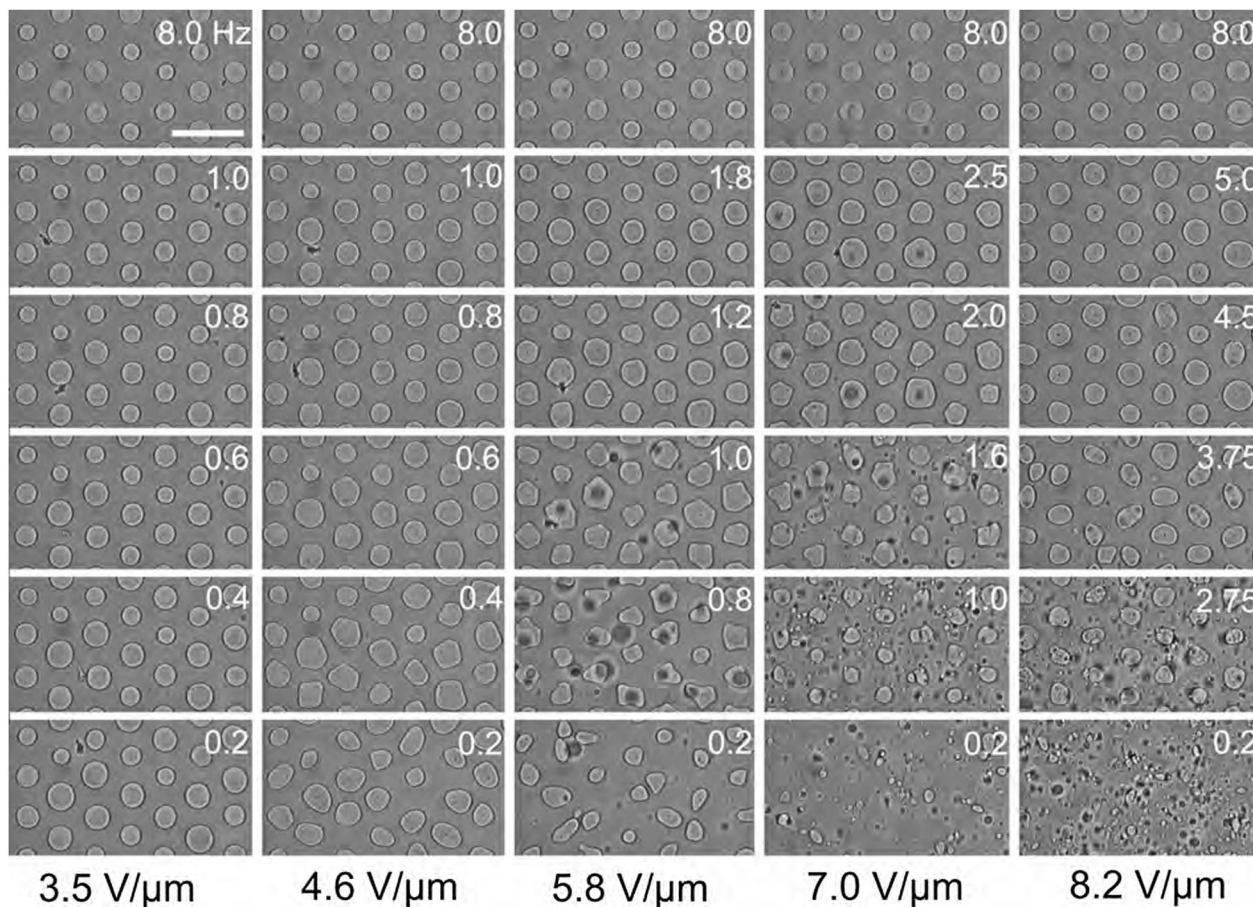


Fig. 4 Order-to-disorder phase transition of the silicone oil array, surrounded by castor oil, by decreasing the frequency (top to bottom) and increasing the strength (left to right) of an AC electric field. The darker spots are out of focus droplets. A snapshot from each value of amplitude and frequency may be seen in ESI[†] Movie S1. Scale bar is 200 μm ; and the electric field is perpendicular to the page.

The transition from order to disorder is quantified using $\langle \Psi_6 \rangle$ (defined in eqn (6)), and is shown in Fig. 6 for different frequencies and field amplitudes. $\langle \Psi_6 \rangle$ is close to 1 for all field amplitudes at a frequency of 8 Hz; the small deviation from 1 at this frequency comes from a small asymmetry in the lattice. $\langle \Psi_6 \rangle$ decreases from 1 as frequency is decreased: there is a noticeable decrease already at 6 Hz for $E = 8.2 \text{ V } \mu\text{m}^{-1}$, while for $E = 8.2 \text{ V } \mu\text{m}^{-1}$, the decrease in $\langle \Psi_6 \rangle$ is only noticeable below 1 Hz. At high enough fields or low enough frequency, strong EHD flows result in the loss of drops due to escape or breakup. Because $\langle \Psi_6 \rangle$ depends on the existence of an intact neighborhood, it is not so useful in characterizing the disordered state. To quantify this state, we examine next orientational and translational dynamics, both of which are accessible *via* single-drop quantities.

4.3 Orientational dynamics of drops

Having measured roundness, we next look at the dynamics of deviation of the lateral shape of a drop from roundness. For small fluctuations, each drop can be treated as an ellipse with a major and minor axis. We follow the orientational dynamics of drops as a function of frequency and amplitude, using the auto-correlation of angular variation in ellipticity of the drop.

The auto-correlation function, $C(t)$, with respect to $t = 0$, *i.e.*, $C(t) = \cos(\theta - \theta_0)$, where θ and θ_0 are the angles of the fitted ellipse on the binary drop at times t and t_0 , respectively. Then, in the frame of interest, a spatial average of $C(t)$ over all the drops is calculated. An example, at $8.2 \text{ V } \mu\text{m}^{-1}$ and 4 Hz, is shown in Fig. 7(a): here the correlation decays rapidly to a value close to zero in around 10 s. Note that $C(t)$ can be negative, but the negative values are small. Other methods to analyze image time series exist; one example is differential variance analysis reported in ref. 53. We find that this analysis results in characteristic times that are comparable to those obtained using the above orientational correlation analysis (see Fig. S1 in ESI[†]).

The decay of $C(t)$ shows no clear functional form (it is neither exponential nor a power law) but if one identifies $C(t)$ as a dynamic order parameter, there is a characteristic time $t = \tau$ when $C(t)$ reaches a fraction 0.5 of its maximum value of 1, and one can then plot τ versus $1/f$ (Fig. 7(b)).

The “universal” low curve for all fields (corresponding to a straight line with a slope of 1, *i.e.*, $\tau \sim 1/f$) is an intrinsic limit: we cannot probe shorter times due to the stroboscopic imaging. For low τ (*i.e.* at high frequency or low $1/f$), the drops are essentially static. At each field amplitude, as the drop is driven more strongly by lowering frequency, the timescale increases

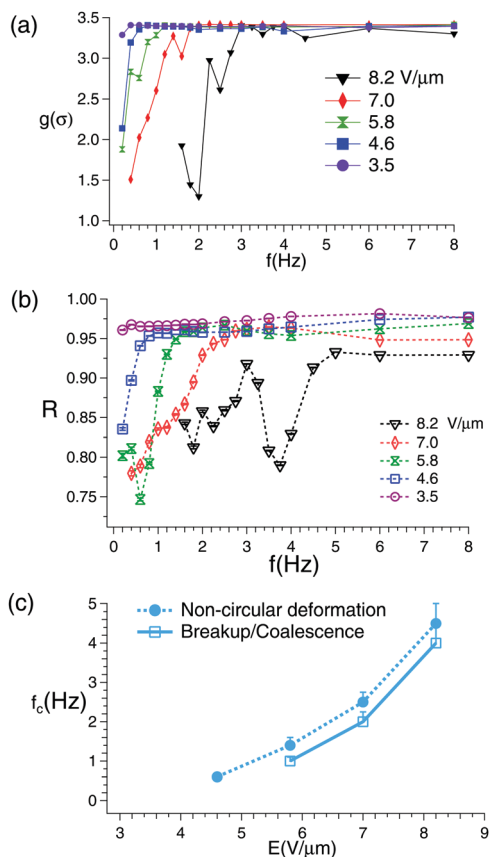


Fig. 5 (a) The height of the first peak of the $g(r)$, i.e. $g(\sigma)$ where σ is the nearest-neighbor distance versus frequency and for different field amplitudes. $g(\sigma)$ decrease with decreasing frequency for each field amplitude. (b) Roundness, R , as a function of frequency and field amplitude. For a perfect circle drop, roundness is close to 1. R decreases with either increasing field amplitude or decreasing frequency, with a low value of about 0.75. (c) The characteristic frequency, f_c , versus field amplitude, for non-circular deformation (filled circles) and for breakup (squares). f_c in all cases increases with field amplitude.

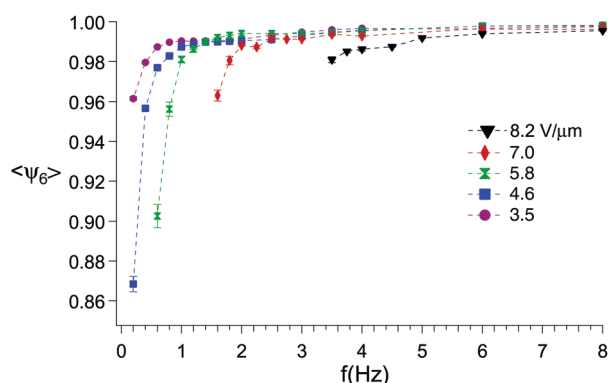


Fig. 6 Average local bond-orientational order parameter $\langle \Psi_6 \rangle$ versus frequency and for each field amplitude. The 6-fold symmetry decreases by lowering the frequency.

(very significantly for $E = 8.2 \text{ V } \mu\text{m}^{-1}$ and less so for lower amplitudes) and then decreases again. As an example, at $E = 8.2 \text{ V } \mu\text{m}^{-1}$, the peak in τ occurs at 0.25 s, correlating

very well with the minimum in roundness in Fig. 5(b). The subsequent decrease in τ at lower frequency corresponds to breakup of the drop, and consequent decrease in electric Capillary number.

4.4 Long-time dynamics: translational dynamics of drops

The translational dynamics of drops as a function of frequency and amplitude was studied by measuring the mean-squared displacement (MSD) of drop centroids. Fig. 8(a) shows the trajectory of each drop in a small region consisting of 7 drops over 600 s for four different frequencies, 0.2, 0.6, 1.0, and 1.4 Hz at $E = 5.8 \text{ V } \mu\text{m}^{-1}$. It is clear that the trajectories are most localized at 1.4 Hz and the least localized at 0.2 Hz. The mean-squared displacement (MSD) of the entire drop array, for the same frequencies and amplitude, is plotted in Fig. 8(b). Since we employ stroboscopic imaging, the minimum time we can probe (for $t > 0$) is $t = 1/f$. The maximum time probed (600 s) is much longer than the typical orientational decay times of interest, which are of the order 10 s or less. We observe that for each frequency, the MSD increases linearly until it saturates. With increasing frequency, the saturation value of the MSD decreases. This is consistent with the localization of trajectories seen in Fig. 8(a).

For translational dynamics of charge-stabilized colloidal particles in a crystalline suspension, the individual particle dynamics is constrained by the harmonic interactions with its neighbors. In the colloidal study of Weiss *et al.*,⁴⁹ this behavior

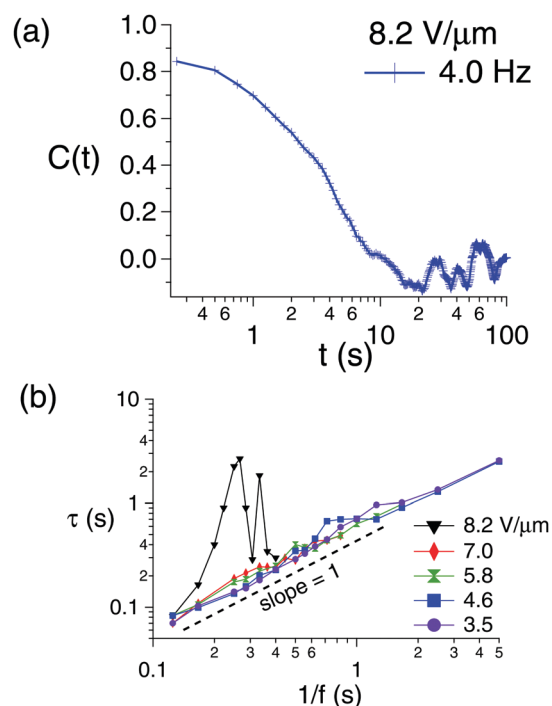


Fig. 7 (a) The auto-correlation function, $C(t)$, at $E = 8.2 \text{ V } \mu\text{m}^{-1}$ and $f = 4 \text{ Hz}$. $C(t)$ decays from 1 at $t = 0$ s to a value close to zero in roughly 10 s. (b) Identifying $C(t)$ with a dynamic order parameter, the characteristic time τ when $C(t)$ reaches a fraction 0.5 of its maximum value of 1 is plotted against $1/f$. The slope of 1 corresponds to $\tau = 1/f$, which is an intrinsic lower limit of measurable τ .

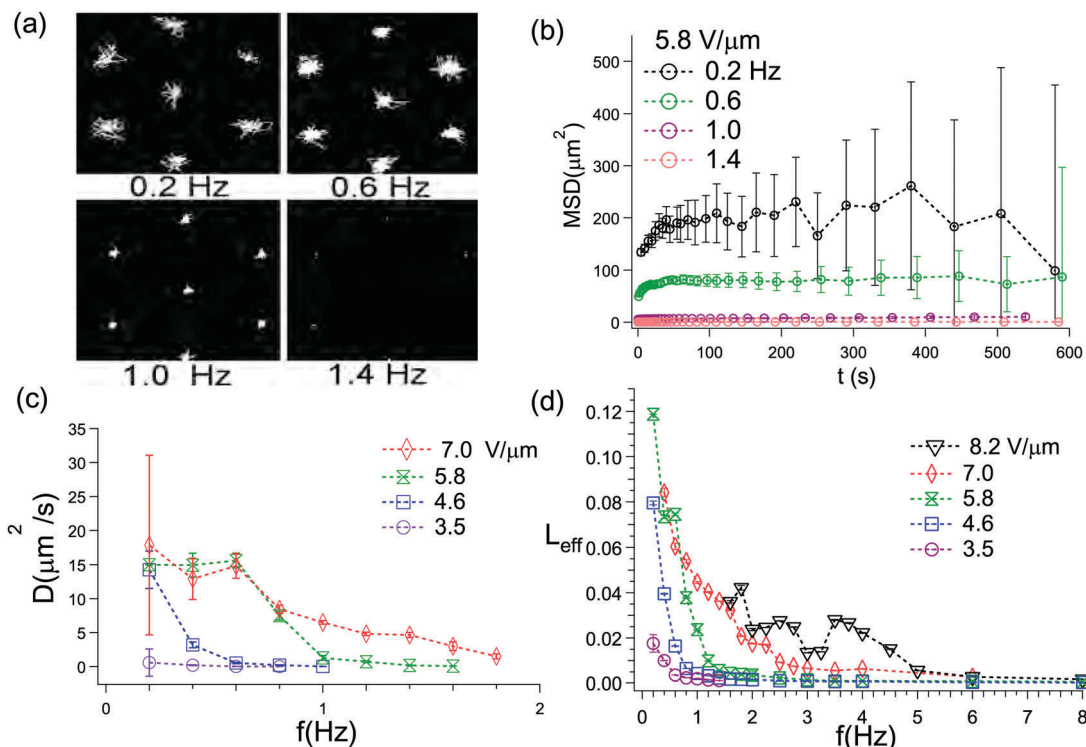


Fig. 8 (a) Trajectories of droplets over 600 s ($E = 5.8 \text{ V } \mu\text{m}^{-1}$). (b) Mean-squared displacement (MSD) of the droplets in (a). (c) Self-diffusion coefficient obtained for different field amplitudes and frequencies. (d) Effective Lindemann parameter, L_{eff} , for all frequencies and amplitudes. With increasing field amplitude, the transition from order to disorder occurs at higher frequencies.

has been analyzed as the combination of diffusive particle motion and harmonic (elastic) restoring force. In our system, a similar restoring force from the negative F_{DEP} , attracts the drops to the ITO-free regions. In the colloidal crystal, each colloidal particle diffuses with a self-diffusion coefficient, D , but is constrained by the potential of mean force.

In our droplet system, the diffusion of droplets is provided by hydrodynamic interactions, characterized by the fractional dynamics in the outer fluid shown in Fig. 10, which tends to free the drops from their trapped potential. Decreasing the frequency increases the range of the hydrodynamic interactions, and thus enhances the effective-diffusive contribution. We can thus use the formalism represented by eqn (7)–(9) to extract effective self-diffusion coefficients D and Lindemann parameter L_{eff} as we disorder the droplet lattice by EHD forces.

The self-diffusion coefficient, D versus frequency f for various field amplitudes, shown in Fig. 8(c), allows us to cross-check some assumptions. While the data for self-diffusion are limited at short times, we nevertheless can obtain reasonable data for $f < 2 \text{ Hz}$ and at all field amplitudes except $E = 8.2 \text{ V } \mu\text{m}^{-1}$, due to breakup events that have an onset at higher frequencies, which make the identification of the patterned drops difficult. There is a common plateau, for $E > 3.5 \text{ V } \mu\text{m}^{-1}$, at around $15 \mu\text{m}^2 \text{ s}^{-1}$. Given that the orientational correlations have a lifetime τ of between 0.1 and 10 s, this implies that the contribution of drop deformation to the centroid MSD is of order $D\tau \sim 7\text{--}70 \mu\text{m}^2$. As can be seen in Fig. 8(a), the low-frequency results are those where the MSD plateaus at a value

larger than this, *i.e.*, true translational dynamics dominates, while at higher frequencies, orientational and translational dynamics are not clearly separable in the mean-square displacements. The plateau diffusion coefficient of $15 \mu\text{m}^2 \text{ s}^{-1}$ (Fig. 8(c)) corresponds to a thermal system with an effective temperature $T_{\text{eff}} = 6\pi\eta_{\text{ex}}aD/k_{\text{B}} \sim 4 \times 10^8 \text{ K}$.

The effective Lindemann parameter, L_{eff} , is shown in Fig. 8(d). With decreasing frequency, a transition from $L_{\text{eff}} \simeq 0$ to values greater than zero is seen at a characteristic frequency, f_c , for each field amplitude. f_c is plotted versus field amplitude in Fig. 11. The regime of strong hydrodynamics is expected to occur at higher frequencies with increasing field amplitudes, consistent with Fig. 8(d). ESI,† Movie S2 shows the dynamics of a sub-region of a lattice of drops very close to the threshold of drop breakup. Two values of f_c when $L_{\text{eff}} \geq 0.01$ and 0.02 are considered for possible correspondence with the characteristic frequencies for non-circular deformation and breakup in Fig. 5(b), because all the L_{eff} are observed to increase in that range.

For comparison, Zahn and Maret⁵⁴ saw melting manifest itself as a second rise of the MSD (they refer to this as γ_{L}) above the plateau value beyond a critical value of an interaction strength. This critical plateau value of MSD is around $0.02\text{--}0.03d_{\text{nn}}^2 \sim (0.15d_{\text{nn}})^2$. The static Lindemann parameter (in units of d_{nn}) is generally of order 0.1 at the onset of melting in 2D.^{55,56} While this particular criterion for melting is not valid in usual 2D melting because it diverges in the crystal as well, in the current study, *i.e.*, a crystal with an imposed lattice (and fluctuations suppressed), it is probably a reasonable disorder parameter.

It should be noted that our measurements contain self-selection: only drops that remain trapped are included in either R or L_{eff} . Therefore, the measurements of the trapped-drop lattice are a very good representation of the entire system in the ordered state, but less so as one approaches the onset of melting. We observe that L_{eff} increases to a maximum value of about 0.08 for $E = 4.6 \text{ V } \mu\text{m}^{-1}$ and $E = 7.0 \text{ V } \mu\text{m}^{-1}$, and to 0.12 for $E = 5.8 \text{ V } \mu\text{m}^{-1}$. These increases occur in the frequency range $\sim 0.2\text{--}0.4 \text{ Hz}$. Shown in ESI,† Movie S3 is the dynamics at 0.2 Hz for $E = 4.6 \text{ V } \mu\text{m}^{-1}$ and $E = 5.8 \text{ V } \mu\text{m}^{-1}$. For $E = 4.6 \text{ V } \mu\text{m}^{-1}$ ($\text{Ca}_E^0 \simeq 0.48$), there is no drop breakup, and the lattice is near the disorder threshold: further lower frequency would correspond most closely to the straightforward phenomenon of lattice melting. At the higher amplitude, most of the original drops have broken into tiny droplets, and the lattice is melted concurrently.

Next, we discuss the role of drop breakup at higher Ca_E^0 . Breakup (Fig. 8(d)) already begins at the low value of $L_{\text{eff}} \approx 0.02$ for field amplitudes $E = 5.8 \text{ V } \mu\text{m}^{-1}$ ($\text{Ca}_E^0 \simeq 0.76$) and higher. Note that this corresponds to frequencies $f \sim 1 \text{ Hz}$, 2 Hz, and 4 Hz, respectively for $E = 5.8 \text{ V } \mu\text{m}^{-1}$, $7 \text{ V } \mu\text{m}^{-1}$, and $8.2 \text{ V } \mu\text{m}^{-1}$, which is very close to the thresholds that can be identified with first breakup in the image panels in Fig. 4, and the threshold frequencies obtained in the roundness plot (Fig. 5(b)). Since we are only tracking the dynamics of the trapped drops, there are numerous unrecorded smaller droplets generated after breakup which are moving much faster. Shown in ESI,† Movie S4 is the dynamics at 0.8 Hz and 1.6 Hz for $E = 7.0 \text{ V } \mu\text{m}^{-1}$. At both frequencies, there is simultaneously an increase in drop breakup and drop translational motions.

At higher driving, the system re-adjusts, *via* drop breakup, to lower Ca_E^0 by reducing the trapped drop size, and thus the system remains at the threshold of disorder without the lattice melting. In addition, at $E = 8.2 \text{ V } \mu\text{m}^{-1}$ ($\text{Ca}_E^0 \simeq 1.5$), the circular-to-noncircular transition occurs without faceting (as observed in the right panel ESI,† Movie S5 at 3.5 Hz), and the frequency threshold (4 Hz) is much closer to the crossover of 6 Hz, thus implying a mechanism of drop breakup that has a much stronger dipolar contribution.

A strong correlation between $\langle \Psi_6 \rangle$ and L_{eff} is observed in Fig. 9. $\langle \Psi_6 \rangle \simeq 1$ deviates from 1 to lower values as L_{eff} increases. While either parameter is useful in characterizing disorder, L_{eff} is practically easier to obtain from our image time series, as it depends on single-particle trajectories.

4.5 Short-time dynamics: the underlying flow mechanism

Prior to the drop deformation experiments, non-stroboscopic experiments were carried out in emulsions with castor oil seeded with fluorescent PMMA tracer particles with diameter of $\sim 1 \mu\text{m}$. After an external AC electric field is imposed, the MSD of PMMA particles around the silicone oil drops was measured for various frequencies and amplitudes. The colloidal particles used are not ideal passive tracers, because a small fraction of these particles tend to adhere to drop interfaces. Thus, it is best to study drop dynamics without tracers; nevertheless, it is informative to first probe the fluid flow of the drops using tracer motions. One can

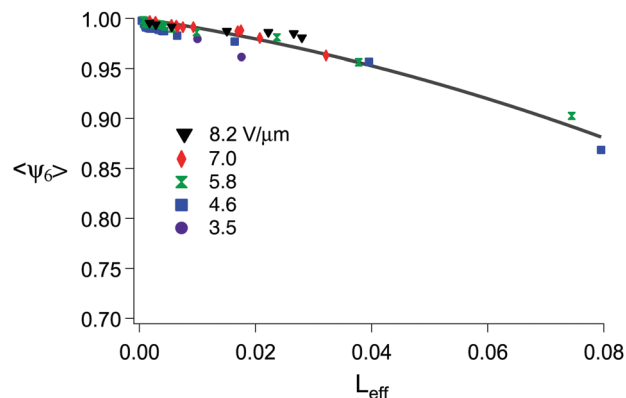


Fig. 9 The average bond order parameter, $\langle \Psi_6 \rangle$ correlates well with L_{eff} . $\langle \Psi_6 \rangle$ is close to 1 where $L_{\text{eff}} \rightarrow 0$, and decreases monotonically with increasing L_{eff} ; the solid line is a guide to the eye. Unlike $\langle \Psi_6 \rangle$, however, L_{eff} can be obtained far into the disordered regime.

write $\text{MSD} \propto t^\gamma$, where $\gamma = 1$ represents diffusive motion while $\gamma > 1$ represents super-diffusive (enhanced) motions. Fig. 10 shows $\log(\text{MSD})$ versus $\log(\text{time})$, at very short times, $0.05 < t < 10 \text{ s}$, for the current system at $30 \mu\text{m}$ above the bottom electrode where $\gamma = 1.42 \pm 0.17$.

Super-diffusive motion with a $\frac{3}{2}$ power law has been observed before in active motor-driven motion inside cells⁵⁷ and ascribed

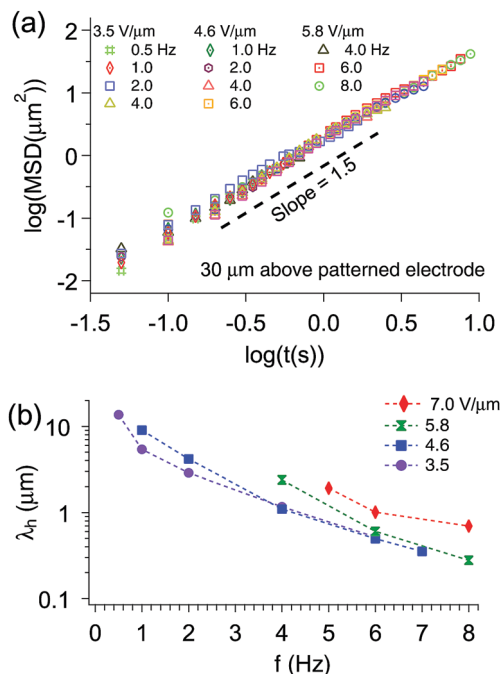


Fig. 10 (a) Fractional tracer particle dynamics in the outer fluid is observed by linearity of a $\log(\text{MSD})$ versus $\log(\text{time})$ plot (the slope yields the power law γ). Data are obtained from an image time series obtained $30 \mu\text{m}$ above the bottom (patterned) electrode, *i.e.*, in the plane of the drop. γ is measured to be equal to 1.42 ± 0.17 , showing enhanced super-diffusive dynamics consistent with a $3/2$ power law that is independent of frequency and field amplitude. (b) From the prefactor K_γ we can construct an experimental hydrodynamic lengthscale $\lambda_h = \sqrt{K_\gamma/f^\gamma}$, which increases with decreasing frequencies.

to Brownian motion in the presence of random fluid velocity fields^{58,59} (alternatively termed fractional Brownian motion⁶⁰). The $\gamma \sim 1.5$ power law for the super-diffusive dynamics of the carrier fluid at very short times, observed in Fig. 10(a), is thus consistent with random velocity fields in the carrier fluid. These random flows would give random kicks to the large drops. Brownian motion in colloidal systems arises from random kicks from solvent molecules at much shorter timescales. The apparent Brownian motion of the drops at long times ($t \gg 1$ s) and large spatial scales (drop diameter of 50 μm) also likely arises from the observed fractional dynamics at short ($0.05 < t < 10$ s) times. We may write

$$\text{MSD} = K_\gamma t^\gamma. \quad (10)$$

Fitting the MSDs with $\gamma = 1.5$, we obtain K_γ , a generalized diffusion constant with units of $\text{m}^2 \text{s}^{-1.5}$. Each $\log(\text{MSD})$ in Fig. 10 was shifted vertically by subtracting $\log(K_\gamma)$ and thus achieving collapse of all the data onto one master curve. We can plot $\lambda_h = \sqrt{K_\gamma/f^\gamma}$, which gives us a (frequency- and amplitude-dependent) lengthscale that is the experimental analog of the hydrodynamic lengthscale introduced in Fig. 2(a). The distances traveled by tracer particles in the outer fluid between successive images are a meaningful lengthscale flow between trapped drops for the stroboscopic imaging of drops employed in the remainder of this work. It should be noted that λ_h is difficult to measure under strong driving conditions, but $\lambda_h < l_h$ in all cases where it is measurable.

5 A non-equilibrium field–frequency phase diagram

The structural study of order to disorder in Section 4.2 found first a loss of circularity, and then a second characteristic frequency that we identified with the first incidence of drop breakup. The increase in f_c (corresponding to either drop deformation or breakup) with E is nonlinear and not fittable to a quadratic E^2 dependence that would be expected from a dipolar system. Indeed, the importance of hydrodynamic flows (*i.e.*, interactions beyond dipolar) is seen clearly in the super-diffusive $t^{3/2}$ tracer particle motions in the outer fluid that is observed (Fig. 10) even when there is minimal drop deformation; *e.g.*, at 8 Hz and $E = 5.8 \text{ V } \mu\text{m}^{-1}$.

In Fig. 11, we see that these characteristic frequencies that we identified with a transition from circular to non-circular shape and for a transition into the drop breakup regime (Fig. 5(b)) correspond rather closely to those from translational dynamics (Fig. 8(d)) when $L_{\text{eff}} = 0.01$ and 0.02, respectively. This correspondence is only strictly valid at amplitudes of $E = 4.6 \text{ V } \mu\text{m}^{-1}$ and above; *i.e.*, $\text{Ca}_E^0 \simeq 0.5$. No breakup is observed for lower amplitudes.

On the other hand, L_{eff} continues to increase at low frequencies, and a higher L_{eff} near 0.08 likely corresponds to an approach to melting, given that the Lindemann criterion used in Gilvary⁵⁵ is directly applicable to the 2D lattice in this study where fluctuations in the mean lattice position are suppressed

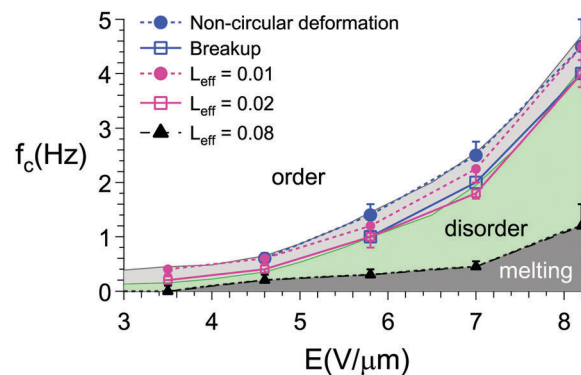


Fig. 11 Characteristic frequencies obtained for a transition from circular to non-circular shape (blue filled circles) and for a transition into the drop breakup regime (blue open squares) correspond rather closely (at field amplitudes larger than $E = 4.6 \text{ V } \mu\text{m}^{-1}$ and $\text{Ca}_E^0 \geq 0.5$) to those from translational dynamics when $L_{\text{eff}} = 0.01$ (pink filled circles) and 0.02 (pink open squares) respectively. Higher L_{eff} , corresponding to the green region in (f_c, E) space, is the regime of disorder. ESI,† Movie S2 shows dynamics along the threshold (light gray region in the plot). The unshaded region above is the ordered regime. $L_{\text{eff}} \sim 0.08$ –0.12 (dark gray region near bottom) corresponds to a classic criterion for melting.⁵⁵

by the dielectrophoretic trap. This also corresponds visually (see ESI,† Movie S1) to the amplitude and frequency where tiny droplets leave the pattern for $\text{Ca}_E = 0.75$ and higher. The solid black line between $f_c = 0.2$ and 0.45 Hz is close to the criterion for melting; this line is close to the drop deformation transition at the smaller field amplitudes, but is distinctly lower at higher E .

In between, in the green region of the dynamic phase diagram (Fig. 11), the system remains self-organized with drop breakup decreasing Ca_E while keeping the system at the threshold to disorder. In both the regimes of strong driving force (the green region and the dark gray region at the bottom of the phase diagram), the system behaves like a thermal system with an effective temperature $T_{\text{eff}} \sim 10^8 \text{ K}$.

6 Conclusion

Far-from-equilibrium systems for studying two-dimensional disorder exist: examples are shaken granular media²⁷ and complex plasmas.⁶¹ The advantage of the current system is that it is a simple driven, dissipative system with liquid–liquid interfaces where there are two continuously variable parameters with which to directly control the strength and range of hydrodynamic interactions. In addition, it is a real-space far-from-equilibrium system which affords the possibility of droplet trapping (*via* dielectrophoresis in this case), thus providing a great degree of control of droplet shape and kinetics.

We note the similarities and differences to a de-pinning transition.⁶² In a typical de-pinning transition, there is a steady driving force that drives the system from pinned to moving, often in coherence. In this system, the driving force is not coherent, but is itself pseudo-random and thus mimics thermal motion; thus increasing the driving force resembles increasing the temperature. This is in contrast with a field-induced dipolar

system, where increasing the driving force resembles a *decrease* in temperature.

How is fractional tracer dynamics consistent with the apparent Brownian motion of granular drops? Super-diffusive dynamics is observed at short times ($0.05 < t < 10$ s), and at longer times these pseudo-random flows result in giving the drops random kicks that can feasibly resemble Brownian motion at much longer times (seconds to minutes). All the drop dynamics and the emergent effective thermodynamics analyzed in this work thus likely arise from these underlying pseudo-random fluid flows in the outer fluid of the oil-in-oil emulsion.

In this system, we are able, at intermediate field amplitudes $Ca_E^0 \sim 0.5$, to approach a pure disordered state by lowering frequency f with no interference from drop breakup processes. At higher field amplitudes, $Ca_E^0 \geq 0.75$, drop breakup and disordering are concurrent processes as f decreases. Indeed, rather than disordering the lattice with increased driving force, tiny droplets break off from the large drop (decreasing its Ca_E), and the large-drop lattice restabilizes. Thus, the system self-organizes to remain at the disorder threshold. This process goes on until the effective Lindemann parameter $L_{\text{eff}} \sim 0.08$ (dark gray regime at the bottom of the phase diagram), at which point the lattice melts.

Conflicts of interest

There are no conflicts to declare.

Acknowledgements

We thank Shankar Ghosh for suggestions that led to this work. This research was supported by the National Science and Engineering Research Council of Canada (NSERC).

References

- 1 A. Yethiraj, *Soft Matter*, 2007, **3**, 1099–1115.
- 2 D. G. Grier and C. A. Murray, *J. Chem. Phys.*, 1994, **100**, 9088–9095.
- 3 W. K. Kegel and A. van Blaaderen, *Science*, 2000, **287**, 290–293.
- 4 E. R. Weeks, J. C. Crocker, A. C. Levitt, A. Schofield and D. A. Weitz, *Science*, 2000, **287**, 627–631.
- 5 U. Gasser, E. R. Weeks, A. Schofield, P. N. Pusey and D. A. Weitz, *Science*, 2001, **292**, 258–262.
- 6 A. Yethiraj and A. van Blaaderen, *Nature*, 2003, **421**, 513–517.
- 7 D. Strickland, Y. Lin, E. Wagner, C. M. Hope, J. Zayner, C. Antoniou, T. R. Sosnick, E. L. Weiss and M. Glotzer, *Nat. Methods*, 2012, **9**, 379–384.
- 8 T. E. Kodger, R. E. Guerra and J. Sprakel, *Sci. Rep.*, 2015, **5**, 14635.
- 9 P. S. Mohanty, P. Bagheri, S. Nöjd, A. Yethiraj and P. Schurtenberger, *Phys. Rev. X*, 2015, **5**, 011030.
- 10 Y. Yang, L. Fu, C. Marcoux, J. E. S. Socolar, P. Charbonneau and B. B. Yellen, *Soft Matter*, 2015, **11**, 2404–2415.
- 11 M. Pichumani, P. Bagheri, K. M. Poduska, W. González-Viñas and A. Yethiraj, *Soft Matter*, 2013, **9**, 3220.
- 12 J. Dobnikar, A. Snezhko and A. Yethiraj, *Soft Matter*, 2013, **9**, 3693–3704.
- 13 L. Addadi, S. Raz and S. Weiner, *Adv. Mater.*, 2003, **15**, 959–970.
- 14 P. Vukusic, B. Hallam and J. Noyes, *Science*, 2007, **315**, 348.
- 15 M. Adams, Z. Dogic, S. L. Keller and S. Fraden, *Nature*, 1998, **393**, 349–352.
- 16 F. M. van der Kooij, K. Kassapidou and H. N. W. Lekkerkerker, *Nature*, 2000, **406**, 868–871.
- 17 A. van Blaaderen, *Nature*, 2006, **439**, 545–546.
- 18 H. Senff and W. Richtering, *J. Chem. Phys.*, 1999, **111**, 1705–1711.
- 19 D. Paloli, P. S. Mohanty, J. J. Crassous, E. Zaccarelli and P. Schurtenberger, *Soft Matter*, 2013, **9**, 3000.
- 20 U. Dassanayake, S. Fraden and A. van Blaaderen, *J. Chem. Phys.*, 2000, **112**, 3851.
- 21 S. Jiang, Q. Chen, M. Tripathy, E. Luijten, K. S. Schweizer and S. Granick, *Adv. Mater.*, 2010, **22**, 1060–1071.
- 22 E. Bianchi, R. Blaak and C. N. Likos, *Phys. Chem. Chem. Phys.*, 2011, **13**, 6397.
- 23 C. P. Brangwynne, P. Tompa and R. V. Pappu, *Nat. Phys.*, 2015, **11**, 899–904.
- 24 A. A. Hyman and K. Simons, *Science*, 2012, **337**, 1047–1049.
- 25 A. Morin, N. Desreumaux, J. Caussin and D. Bartolo, *Nat. Phys.*, 2017, **13**, 63–67.
- 26 C. J. O. Reichhardt and C. Reichhardt, *Nat. Phys.*, 2017, **13**, 10–11.
- 27 R. P. Behringer, K. E. Daniels, T. S. Majmudar and M. Sperl, *Philos. Trans. R. Soc., A*, 2008, **366**, 493–504.
- 28 M. P. Ciamarra, P. Richard, M. Schröter and B. P. Tighe, *Soft Matter*, 2012, **8**, 9731–9737.
- 29 D. W. Howell, R. P. Behringer and C. T. Veje, *Chaos*, 1999, **9**, 559–572.
- 30 A. A. Hyman, C. A. Weber and F. Jülicher, *Annu. Rev. Cell Dev. Biol.*, 2014, **30**, 39–58.
- 31 A. Varshney, S. Ghosh, S. Bhattacharya and A. Yethiraj, *Sci. Rep.*, 2012, **2**, 738.
- 32 A. Varshney, S. Gohil, M. Sathe, S. Rao, J. B. Joshi, S. Bhattacharya, A. Yethiraj and S. Ghosh, *Soft Matter*, 2016, **12**, 1759–1764.
- 33 S. Khajepour Tadavani, J. R. Munroe and A. Yethiraj, *Soft Matter*, 2016, **12**, 9246–9255.
- 34 A. Varshney, S. Gohil, S. Khajepour Tadavani, A. Yethiraj, S. Bhattacharya and S. Ghosh, *Soft Matter*, 2014, **14**, 1330–1335.
- 35 M. Trau, S. Sankaran, D. A. Saville and I. A. Aksay, *Langmuir*, 1995, **11**, 4665–4672.
- 36 N. Wu and W. B. Russel, *Nano Today*, 2009, **4**, 180–192.
- 37 P. G. Oppenheimer, *Electrohydrodynamic patterning of functional materials*, Springer International Publishing, Heidelberg, 2013.
- 38 H. Tian, C. Wang, J. Shao, Y. Ding and X. Li, *Langmuir*, 2014, **30**, 12654–12663.

- 39 J. C. Crocker and D. G. Grier, *J. Colloid Interface Sci.*, 1996, **179**, 298–310.
- 40 G. I. Taylor, *Proc. R. Soc. London, Ser. A*, 1966, **291**, 159–166.
- 41 J. R. Melcher and G. I. Taylor, *Annu. Rev. Fluid Mech.*, 1969, **1**, 111–146.
- 42 S. Torza, R. G. Cox and S. G. Mason, *Philos. Trans. R. Soc., A*, 1971, **269**, 295–319.
- 43 E. K. Zholkovskij, J. H. Masliyah and J. Czarnecki, *J. Fluid Mech.*, 2002, **472**, 1–27.
- 44 J. Q. Feng, *Proc.: Math., Phys. Eng. Sci.*, 1999, **455**, 2245–2269.
- 45 J. O. Bockris, *Modern electrochemistry*, Plenum Press, New York, 2nd edn, 1998.
- 46 C. A. Murray, *Bond-orientational order in condensed matter systems*, Springer-Verlag, New York, 1992.
- 47 A. Yethiraj, A. Wouterse, B. Groh and A. van Blaaderen, *Phys. Rev. Lett.*, 2004, **92**, 058301.
- 48 P. Bagheri, A. M. Almudallal, A. Yethiraj and K. M. Poduska, *Langmuir*, 2015, **31**, 8251–8259.
- 49 J. A. Weiss, A. E. Larsen and D. G. Grier, *J. Chem. Phys.*, 1998, **109**, 8659–8666.
- 50 G. Volpe and G. Volpe, *Am. J. Phys.*, 2013, **81**, 224.
- 51 K. Berg-Sørensen and H. Flyvbjerg, *Rev. Sci. Instrum.*, 2004, **75**, 594–612.
- 52 A. M. Alsayed, M. F. Islam, J. Zhang, P. J. Collings and A. G. Yodh, *Science*, 2005, **309**, 1207–1210.
- 53 R. Pastore, G. Pesce and M. Caggioni, *Sci. Rep.*, 2017, **7**, 43496.
- 54 K. Zahn and G. Maret, *Phys. Rev. Lett.*, 2000, **85**, 3656–3659.
- 55 J. J. Gilvarry, *Phys. Rev.*, 1956, **102**, 308–316.
- 56 P. Dillmann, G. Maret and P. Keim, *J. Phys.: Condens. Matter*, 2012, **24**, 11.
- 57 A. Caspi, R. Granek and M. Elbaum, *Phys. Rev. Lett.*, 2000, **85**, 5655–5658.
- 58 A. Ajdari, *Europhys. Lett.*, 1995, **31**, 69.
- 59 G. Zumofen, J. Klafter and A. Blumen, *Phys. Rev. A: At., Mol., Opt. Phys.*, 1990, **42**, 4601–4608.
- 60 R. Metzler and J. Klafter, *J. Phys. A: Math. Gen.*, 2004, **37**, R161–R208.
- 61 A. V. Ivlev, M. H. Thoma, C. Rath, G. Joyce and G. E. Morfill, *Phys. Rev. Lett.*, 2011, **106**, 155001.
- 62 C. Reichhardt and C. J. Olson Reichhardt, *Rep. Prog. Phys.*, 2017, **80**, 026501.